Intermetallics 144 (2022) 107527

Contents lists available at ScienceDirect

Intermetallics

journal homepage: www.elsevier.com/locate/intermet

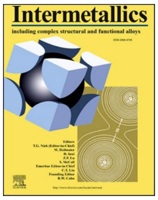

Softening in an ultrasonic-vibrated Pd-based metallic glass

Chenchen Yuan [a,*], Rui Liu [a], Zhuwei Lv [a], Xin Li [b], Changmeng Pang [a], Can Yang [b], Jiang Ma [b,**], Weihua Wang [c,d]

[a] School of Materials Science and Engineering, Jiangsu Key Laboratory for Advanced Metallic Materials, Southeast University, Nanjing, 211189, China
[b] College of Mechatronics and Control Engineering, Shenzhen University, Shenzhen, 518060, China
[c] Institute of Physics, Chinese Academy of Sciences, Beijing, 100190, China
[d] Songshan Lake Materials Laboratory, Dongguan, 523808, China

ARTICLE INFO

Keywords:
Disordered structure
Metallic glass
Ultrasonic-vibration
Creep
Plastic deformation

ABSTRACT

The mechanical behavior of the $Pd_{40}Cu_{30}P_{20}Ni_{10}$ metallic glass after ultrasonic vibration was systematically investigated by nanoindentation. A notable softening after ultrasonic treatment was demonstrated by about 25% and 40% reduction of hardness and elastic modulus, respectively. The Maxwell-Voigt model was utilized to characterize the structure evolution during ultrasonic-assistant plastic deformation. Combined with differential scanning calorimeter experiments, it is found that the flow defects with shorter characteristic relaxation time activated under ultrasonic-frequency cycling loading benefits fast atomic diffusion with a low energy barrier, which eventually leads to the pronounced creep displacement, and thereby the large moldability at ambient temperature. This work might enlighten the structural origin for the plastic flow of metallic glasses under stress-assisted molding, imprinting as well as cold joining, which may help us in deeply understanding the defect activation mechanism in disordered systems.

1. Introduction

Metallic glasses (MGs) exhibit the extremely high strength, hardness (*H*), and excellent corrosion resistance. They are attractive as novel functional structural materials used in the field of three-dimensional (3D) printing, molding, embossing, imprinting, etc. [1,2]. However, the localized strain in shear bands dominates the plastic deformation of most MGs. It leads to the very limited uniaxial tensile plasticity and the consequent catastrophic fracture at ambient temperature, which hinders the wide application of MGs in nanomoulding industries. It has been reported that by means of high-frequency mechanical vibration, the miniature MG parts can be fabricated in an economically competitive way [3,4]. Due to the ultrasonic stress-softening effect and stress superposition effect, ultrasonic vibration with high frequency of above 20 kHz has been conducted widely in metal micro-forming process [5]. However, the underlying physical origin for ultrasonic-assisted plastic deformation of MGs is not well addressed yet. It has been demonstrated that ultrasonic vibration can enhance thermoplastic formability of MGs by reducing resistant stress around their supercooled liquid region [3]. The induced low viscosity during shear punching process illuminates that the ultrasonic-assisted deformation mechanism of MGs distinguishes from the traditional punching technique applied on crystalline metals [4]. It is considered to be associated with the generation of free volume and/or flowing unit volume during cycling loading with high vibration amplitude [3,6]. Whereas, it is still unclear that how are those flow defects distributed in the glassy matrix and its influences on the deformation mechanism, especially in various MG systems.

Pd-based MGs are proposed as potential candidates for ultrasonic-assistant molding/imprinting or cold joining [7] due to its large intrinsic plasticity and high Poisson's ratio of around 0.4 [8–10]. Besides, Pd-based MGs with a relatively low glass transition temperature that close to room temperature and a high oxygen resistance also prefer to be used as model materials in 3D thermoplastic micro-forming [11]. The deformation mechanism including the anelastic behavior of the $Pd_{40}Cu_{30}P_{20}Ni_{10}$ MG has been studied previously by using nanoindentation [12]. The classic relaxation kinetics is observed during the creep deformation of this system, which indicates the high impact of the anelastic deformation on the mechanical performance of Pd-based MGs. However, the inner mechanism for the high-frequency mechanical vibration on the mechanical response, in particular the anelastic

---

* Corresponding author.
** Corresponding author.
E-mail addresses: yuanchenchenneu@hotmail.com (C. Yuan), majiang@szu.edu.cn (J. Ma).

https://doi.org/10.1016/j.intermet.2022.107527
Received 9 August 2021; Received in revised form 20 February 2022; Accepted 28 February 2022

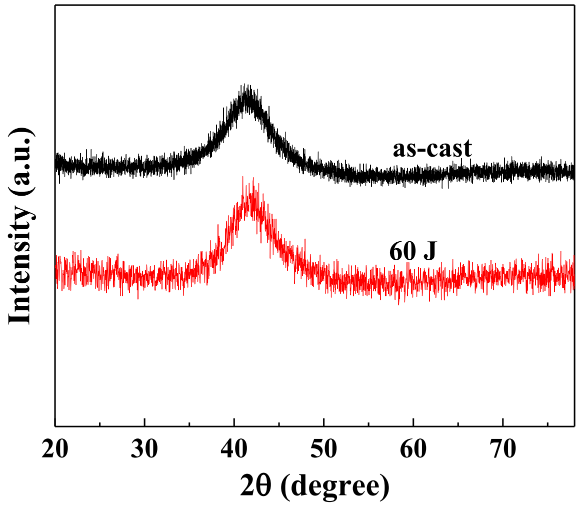

Fig. 1. The XRD of the $Pd_{40}Cu_{30}P_{20}Ni_{10}$ rod before and after 60 J ultrasonic vibration with the applied energy of 60 J.

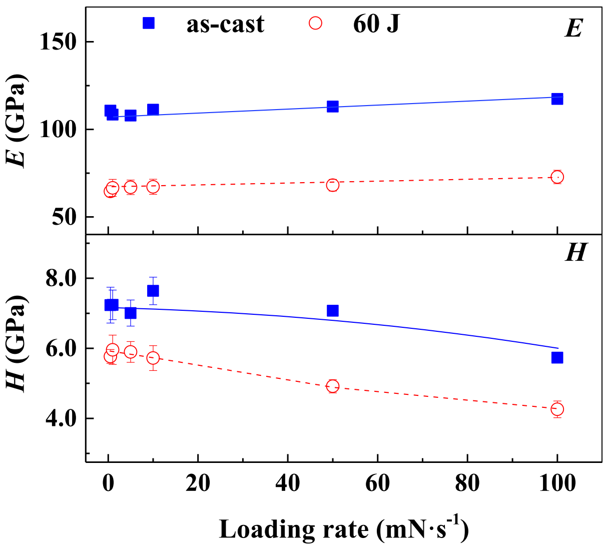

Fig. 2. The hardness *H* and elastic modulus *E* of as-cast and 60 J ultrasonic-vibrated $Pd_{40}Cu_{30}P_{20}Ni_{10}$ MG samples measured as a function of loading rates. The solid and dash lines in are guides for the eyes.

Table 1
Hardness *H* and elastic modulus *E* of as-cast and 60 J ultrasonic-vibrated $Pd_{40}Cu_{30}P_{20}Ni_{10}$ MGsamples measured at different loading rates.

Loading rate (mN/s)	*H* (GPa)		*E* (GPa)	
	As-cast	60 J	As-cast	60 J
0.5	7.2 ± 0.5	5.8 ± 0.2	111 ± 2	65 ± 3
1	7.2 ± 0.4	6.0 ± 0.4	108 ± 1	67 ± 5
5	7.0 ± 0.3	5.9 ± 0.3	108 ± 2	67 ± 4
10	7.6 ± 0.4	5.7 ± 0.3	111 ± 2	67 ± 4
50	7.1 ± 0.1	4.9 ± 0.2	113 ± 1	68 ± 3
100	5.7 ± 0.1	4.3 ± 0.2	117 ± 2	73 ± 4

contribution, of this MG system at ambient temperature is still unrevealed. Nanoindentation has proven to be an effective approach to determine the mechanical properties of structural materials at the microscopic scale, e.g., *H*, elastic modulus (*E*), as well as time-dependent mechanical response such as indentation creep, and so on [13]. The generation and/or annihilation of defects during the time-dependent anelastic deformation process can be well described by nanoindentation regardless of the restriction of size and shape [14,15], which is especially important for MGs that normally have limited glass forming ability and disordered structure. Therefore, in this work, mechanical properties such as *H*, *E*, and the creep performance of the $Pd_{40}Cu_{30}P_{20}Ni_{10}$ MG before and after the vibration with an ultrasonic frequency of 20 kHz were systematically investigated by using nanoindentation. The anelastic response during creep deformation was characterized by two Kelvin units with two different response time under the frame of two-phase model. The mechanical softening of the $Pd_{40}Cu_{30}P_{20}Ni_{10}$ MG along with the activation of flow defects with short characteristic relaxation time was demonstrated after ultrasonic vibration, which might help us to seek the structural origin of the superplastic flow of Pd-based MGs during the vibration-assistant molding/imprinting process.

2. Experimental

$Pd_{40}Cu_{30}P_{20}Ni_{10}$ samples were prepared with the nominal composition (considering the consumption of P during the induction procedure) by induction melting pure P (99.99 at. %) and the eutectic composition $Pd_{40}Cu_{30}Ni_{10}$ alloys that synthesized by arc-melting of pure Pd (99.99 at. %), Cu (99.999 at. %), and Ni (99.99 at. %) in a high-purity argon atmosphere (>99.99 at. %). The alloy ingot was cast into cylindrical rods with a diameter of 2 mm by using a water-cooled copper crucible and then cut into the length of 1–2 mm. The sample was ultrasonically vibrated by BRANSON 2000X at an energy of 60 J before nanoindentation experiments with the frequency of 20 kHz and the trigger force of 50 N. The amorphous nature and thermodynamics properties of the samples before and after the mechanical vibration were monitored by X-ray diffraction (XRD, Bruker D8 Discover diffractometer) with Cu K_α radiation and NETZSCH 404 F3 differential scanning calorimeter (DSC) at heating rates ranging from 5 to 40 K/min. The micro-creep tests were conducted using a NanoTest Vantage (Micro Materials Ltd) with the load and displacement resolutions of about 750 nN and 0.3 nm, respectively. The top side of specimens was mechanically polished following a conventional procedure with a final step using a 0.5 μm diamond suspension. A standard Berkovich diamond indenter was utilized for nanoindentation tests. The machine compliance calibration for the transducer-tip configuration and tip area functional calibration were performed on a standard fused silica sample before each test. The indentation experiments were carried out at constant loading rates of 0.5, 1, 5, 10, 50, and 100 mN/s to a load limit of 50 mN, followed by a holding period of 100 s, then unloaded at the same rate as the loading rate, see details in ref.15. The thermal drift correction was conducted by using the post-indentation drift calibration method. The sample was unloaded to ~14% of the maximum load (6.8 mN), then held for 20–30 s to derive the thermal drift rate of the instrument. At least five indentation tests were carried out under each condition. The results biased significantly against the others were discarded before further data analysis. The surface morphology around the indents was recorded by Veeco Dimension ICON atomic-force microscopy (AFM). Considering the effect of mechanical polishing on the properties measured on the sample surface [16], a tapping mode were conducted on the matrix material and the material around indents in the region of 10 × 10 μm^2 to quantify the surface roughness. It is found that the root-mean-square roughness of the as-polished specimen ranges between 3.9 and 4.8 nm. Compared to the used nanoindentation tip size as well as the indentation depth at 50 mN, the surface roughness is rather small. The surface roughness has not affected the relative trend of the nanoindentation data.

3. Results and discussion

XRD spectra of as-cast and 60 J ultrasonic-vibrated $Pd_{40}Cu_{30}P_{20}Ni_{10}$ MG samples are presented in Fig. 1. Only a broad peak without

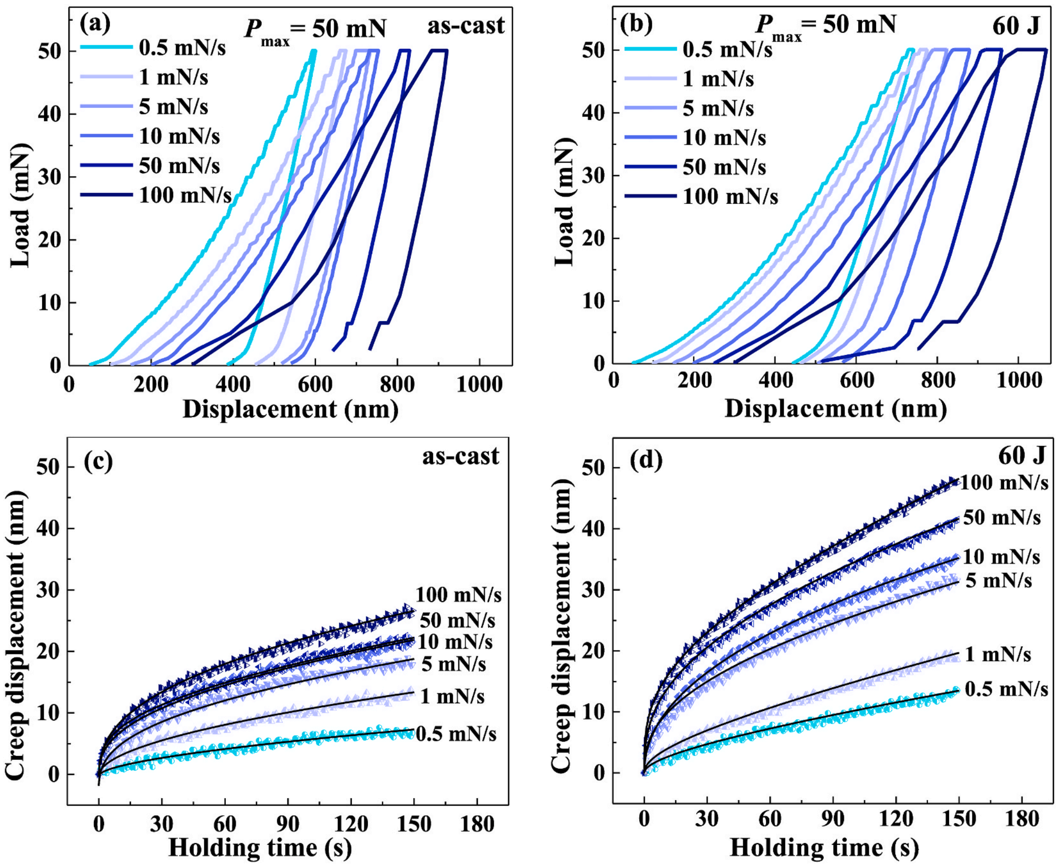

Fig. 3. Load - displacement (P - h) curves of as-cast (a) and 60 J ultrasonic-vibrated (b) $Pd_{40}Cu_{30}P_{20}Ni_{10}$ MG samples under different loading rates with a peak load of 50 mN. The curves in (a) and (b) offset from the origin for clear viewing. The creep displacement and fitting curves of as-cast (c) and 60 J ultrasonic-vibrated (d) $Pd_{40}Cu_{30}P_{20}Ni_{10}$ MGs during the load holding period at different loading rates.

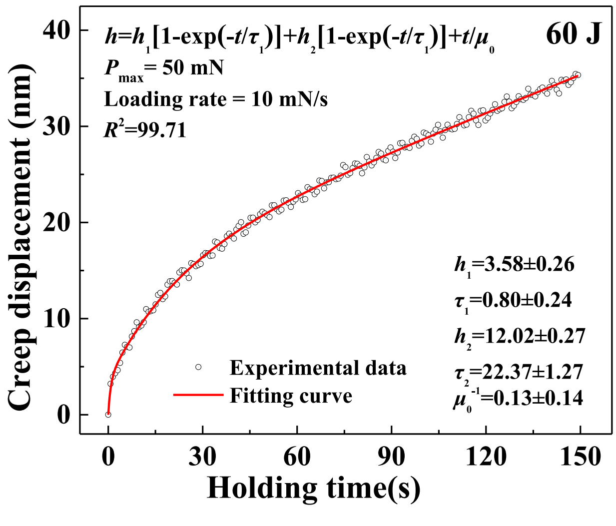

Fig. 4. Experimental and fitted creep displacement curves of the typical ultrasonic-vibrated $Pd_{40}Cu_{30}P_{20}Ni_{10}$ MG at a loading rate of 10 mN/s by using the Maxwell-Voigt model.

crystalline peaks is shown in XRD patterns, which illustrates that no crystallization occurs in the process of ultrasonic vibration. Fig. 2 and Table 1 shows the dependence of H and E on the loading rate for both as-cast and ultrasonic-vibrated samples. The H and E derived from nanoindentation are based on the conventional depth-sensing indentation method of Oliver and Pharr, see details in Ref. [17]. The E of the specimen is derived according to the measured reduced modulus E_r:

$$\frac{1}{E_r}=\frac{1-\nu^2}{E}+\frac{1-\nu_i^2}{E_i} \tag{1}$$

where ν is Poisson's ratio of the specimen, and E_i and ν_i the elastic modulus and Poisson's ratio of the indenter. ν is around 0.4 for the $Pd_{40}Cu_{30}P_{20}Ni_{10}$ MG [8,9]. E_i and ν_i are 1140 GPa and 0.07 for the diamond indenter, respectively. The reduced modulus E_r can be determined by indentation technique:

$$E_r=\frac{\sqrt{\pi}}{2\beta}\frac{S}{\sqrt{A}} \tag{2}$$

where S is the contact stiffness and A the area of indent. β is the constant related to the geometry of the indenter, which is ~1.034 for Berkovich indenter. The H is defined as:

$$H=\frac{P_m}{A} \tag{3}$$

where P_m is the peak load. It seems that E is barely affected by loading rates with a value of about 110 GPa for the as-cast $Pd_{40}Cu_{30}P_{20}Ni_{10}$ MG sample, which is slightly higher than the reported value of 98–100 GPa from acoustic-velocity measurements [8,9]. It is due to the fact that the actual contact area of the indent is larger than the theoretical calculation based on the assumption of a conical indenter instead of the actual pyramidal geometry without considering of the pile-up around the indent normally found in MG specimens [18]. While H of the as-cast sample almost keeps constant value close to 6 GPa at the relatively low loading rate, but gradually decrease to about 4.3 GPa at the load rate as high as 100 mN/s. More interestingly, after the high-frequency vibration with

Table 2
The fitting parameters of creep curves of as-cast and 60 J ultrasonic-vibrated $Pd_{40}Cu_{30}P_{20}Ni_{10}$ MG samples based on the Maxwell-Voigt model.

	Loading rate (mN/s)	h_1 (nm)	τ_1 (s)	h_2 (nm)	τ_2 (s)	μ_0^{-1} (nm s^{-1})
As-cast	0.5	2.8 ± 0.3	1.5 ± 0.4	2.0 ± 0.9	40 ± 27	0.12
	1	1.1 ± 0.3	0.9 ± 0.8	3.6 ± 0.3	21 ± 4	0.14
	5	3.4 ± 0.2	0.4 ± 0.2	7.5 ± 0.3	24 ± 2	0.11
	10	2.9 ± 0.2	0.6 ± 0.3	10.2 ± 0.3	26 ± 2	0.05
	50	5.1 ± 0.3	1.9 ± 0.3	18.5 ± 1.9	53 ± 7	0.04
	100	2.8 ± 0.4	1.3 ± 0.5	9.6 ± 0.4	18 ± 1	0.09
60 J	0.5	0.4 ± 0.7	2.9 ± 6.9	2.5 ± 0.5	21 ± 9	0.07
	1	0.8 ± 0.8	4.4 ± 5.3	5.6 ± 0.5	28 ± 8	0.11
	5	5.2 ± 0.3	1.3 ± 0.2	9.1 ± 0.3	25 ± 2	0.12
	10	3.6 ± 0.3	0.8 ± 0.2	12.0 ± 0.3	22 ± 1	0.13
	50	8.6 ± 0.4	2.4 ± 0.3	11.5 ± 0.4	30 ± 3	0.14
	100	8.7 ± 0.4	1.2 ± 0.2	10.6 ± 0.3	19 ± 1	0.19

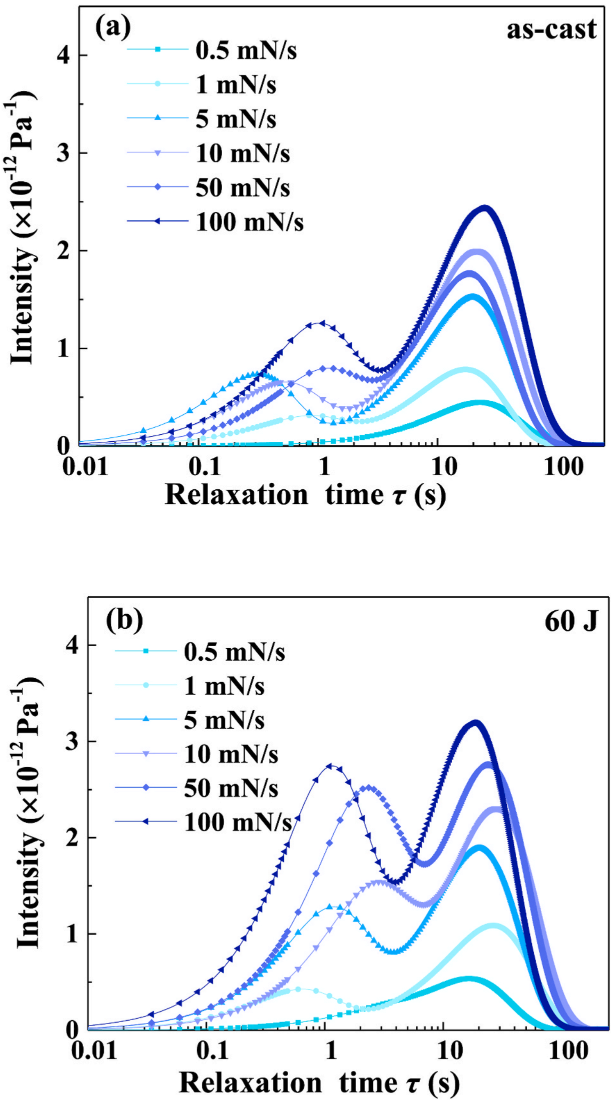

Fig. 5. The relaxation spectra of as-cast (a) and 60 J ultrasonic-vibrated (b) $Pd_{40}Cu_{30}P_{20}Ni_{10}$ MG samples based on the anelastic part of their creep displacement curves at different loading rates.

the energy of 60 J, the *H* and *E* are dramatically reduced by about 25% and 40%, respectively. After vibration treatment, the *E* measured at a loading rate of 10 mN/s rapidly decreases from 111 ± 2 to 67 ± 4 GPa, while the value of *H* falls sharply from 7.6 ± 0.4 to 5.7 ± 0.3 GPa. A remarkable softening upon ultrasonic vibration can be observed in Fig. 2. Such pronounced softening behavior under mechanical vibration has not been found in other MGs such as $Zr_{35}Ti_{30}Cu_{8.25}Be_{26.75}$, where the *H* and *E* are almost unchanged after vibration treatment even with a higher energy of 140 J [18].

The load-displacement (*P*-*h*) curves during nanoindentation of the $Pd_{40}Cu_{30}P_{20}Ni_{10}$ MG before and after vibration treatment are displayed in Fig. 3(a) and (b), respectively, where *P* is the loading force and *h* the instantaneous indenter displacement. The corresponding creep displacement curves during the load holding process with a load limit of 50 mN are shown in Fig. 3(c) and (d). It is seen that the maximum creep displacement of the ultrasonic-vibrated sample at ambient condition is about 48 nm, which is almost twice deeper than 27 nm of the as-cast sample. This indicates that the sample exhibits a higher plasticity and fluidity after the high-frequency mechanical vibration, which is in accordance with the reduction of *H* and *E* of the ultrasonic-vibrated sample as demonstrated in Fig. 2. Consistent with the observations in other MGs such as Zr- [18], Cu-Zr [19], and Fe (Co)-based MGs [15,20–22], the maximum creep displacement of the Pd-based MG (before and after vibration treatment) during the load holding period presents a high loading-rate sensitivity, which increases from less than 5 to close to 50 nm with increasing loading rates from 0.5 to 100 mN/s.

A pronounced serration is observed in both as-cast and ultrasonic-vibrated MGs during the initial loading process, which demonstrates a typical pop-in behavior [23], see Fig. 3 (a) and (b). This phenomenon gradually vanishes at loading rates higher than 50 mN/s, indicating a transition from serrated to non-serrated flow [23]. The disappearance of serration phenomenon is due to the fact that the high-rate regime of homogeneous flow on the deformation map of MGs forces strain distribution kinetically [24]. Such homogeneous deformation under nanoindentation even well below the glass transition suggests that the applied machine cross-head velocity overwhelms the shear velocity of an individual shear band at this point [25]. In other word, the arrested shear band can be continuously driven at the defined rate. It means that the shear band relaxation corresponding to the structural rearrangement [26] needs to be taken into account during the initial loading process. Compared with the as-cast sample, less notable serration behavior of the ultrasonic-vibrated MG with a smaller stress-drop step at the same loading rate is demonstrated in Fig. 3 (a) and (b). It illustrates a more homogeneous deformation of the Pd-based MG after the vibration treatment. This is in agreement with its pronounced creep behavior along with low *H* and *E*. Such pop-in behavior has not been found during the holding period. It implies that the propagation of individual shear bands seems to be impeded in the creep process, where the loading rate (close to 0) is far inferior to the characteristic rate for the shear band nucleation.

Due to the chemical inhomogeneity and density fluctuation of multicomponent MGs, it is proposed that the glassy matrix of most MGs can be characterized by strongly and weakly bonded regions based on the two-phase model [27,28]. Thus, two Kelvin units connected in series with a Maxwell unit [29] that relate to two relaxation processes with different relaxation time under the frame of the core-shell model [28] are utilized to model the two-phase structure of MG systems [30–33]:

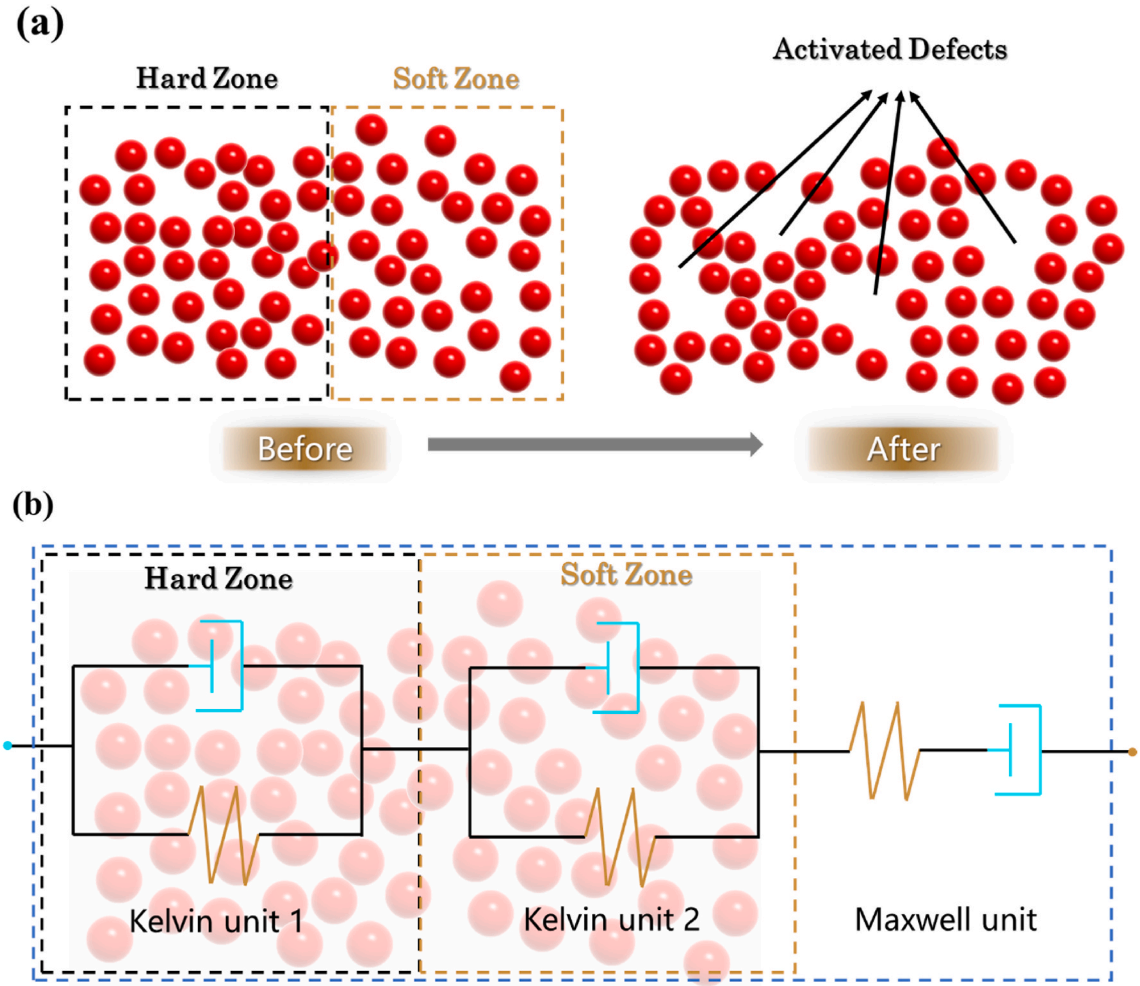

Fig. 6. A schematic diagram for the distribution of defects before (a) and after (b) ultrasonic vibration in the $Pd_{40}Cu_{30}P_{20}Ni_{10}$ MG.

$$h = h_1\left(1 - e^{-t/\tau_1}\right) + h_2\left(1 - e^{-t/\tau_2}\right) + t/\mu_0 \tag{4}$$

where the parameters h_1, τ_1 and h_2, τ_2 correspond to two discrete anelastic deformation processes based on the Maxwell-Voigt model [29], which represent the displacement and relaxation time of the first and second Kelvin units, respectively. $\mu_0{}^{-1}$ is a viscous constant related to the Maxwell unit. The fitted creep displacement curves are plotted in Fig. 3 (c) and (d) as well for comparison. The correlation coefficient R^2 is more than 99%, see the typical example of the ultrasonic-vibrated sample at the loading rate of 10 mN/s in Fig. 4. It confirms that the creep curves of two MGs can be described accurately by using the Maxwell-Voigt model.

For comparing clearly, the fitting parameters for the creep displacement-time (*h-t*) curves of the as-cast and ultrasonic-vibrated samples at different loading rates are listed in Table 2. It can be seen that the value of τ_1 and τ_2 of the as-cast Pd-based MG is close to that reported in other MGs such as $Mg_{85}Cu_5Y_{10}$ [14] and $Zr_{35}Ti_{30}Cu_{8.25}Be_{26.75}$ [18]. After the vibration treatment, the displacement during primary and secondary relaxation processes of the sample, h_1 and h_2, increases significantly with elevated loading rates at a low loading rate regime, accompanied by cutting down the characteristic relaxation time τ_1 and τ_2 from 4.4 ± 5.3 to 0.8 ± 0.2 and 28 ± 8 to 22 ± 1 s, respectively, i.e., both τ_1 and τ_2 of the as-cast sample shift to the short time range. With further increasing loading rates to the value that higher than 50 mN/s, h_1 and h_2 that represent the displacement during two discrete relaxation processes show a minor change, exhibiting a steady flow behavior. It is noteworthy that the displacement during the second relaxation process h_2 increases strikingly with elevated loading rates, especially for the as-cast sample. The h_2 of as-cast and ultrasonic-vibrated MG samples increases from about 2.0 ± 0.9 to 18.5 ± 1.9 nm and 2.5 ± 0.5 to 12.0 ± 0.3 nm, respectively. Compared with the as-cast sample, the value of h_2 for the 60 J ultrasonic-vibrated sample is slightly higher at loading rates less than 10 mN/s. With increasing loading rates from 0.5 to 100 mN/s, the displacement during the secondary relaxation, h_2, of the as-cast sample becomes more pronounced. However, the h_1 of the ultrasonic-vibrated sample is more sensitive to loading rates than that of the as-cast sample., the h_1 of the sample after the vibration treatment increases from 0.4 ± 0.7 to 8.7 ± 0.4 nm along with elevated loading rates, while that of the as-cast sample only increases from 1.1 ± 0.3 to 5.1 ± 0.3 nm. It implies that the primary relaxation process rather than the second relaxation process plays a more crucial role in determining the pronounced creep deformation of high-frequency mechanical-vibrated MGs.

Meanwhile, $\mu_0{}^{-1}$ that represents the ability of the viscoplastic deformation in MGs increases progressively from 0.07 to 0.19 nm s^{-1} with increasing loading rates for the ultrasonic-vibrated sample, demonstrating a softening behavior with a reduction of the viscous constant μ_0 at a higher loading rate. This agrees well with the reduction of *H* at the same load rate, see Fig. 2 and Table 1. While $\mu_0{}^{-1}$ of the as-cast sample, on the contrary, falls from 0.14 to 0.04 nm s^{-1} upon increasing loading rates from 1 to 50 mN/s. A weak work hardening behavior with a remarkable increase of viscosity under the low-velocity impact is found in the as-cast Pd-based MG, which slightly differs from

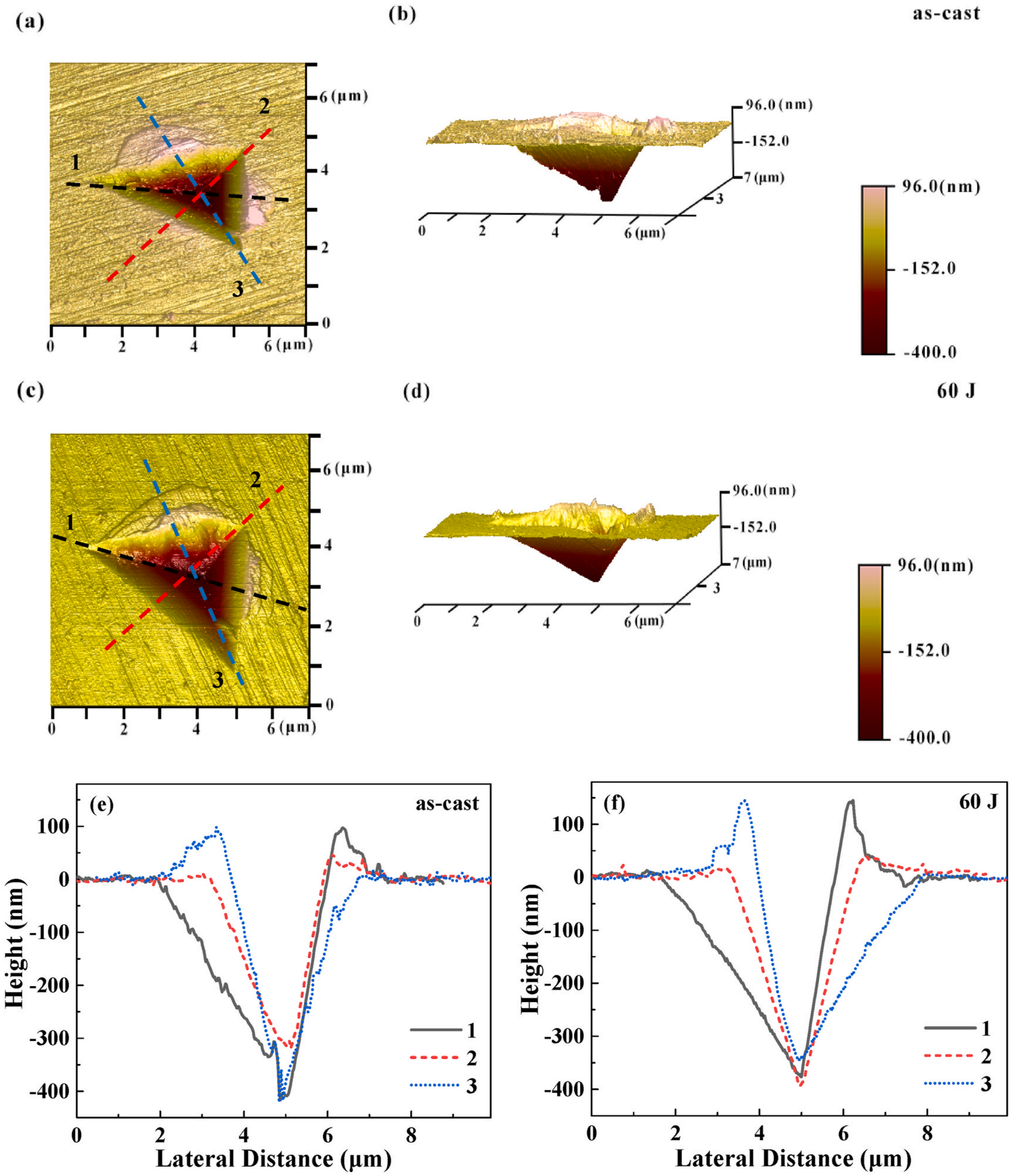

Fig. 7. AFM image of as-cast (a, b) and 60 J ultrasonic-vibrated (c, d) $Pd_{40}Cu_{30}P_{20}Ni_{10}$ MG samples under the nanoindentation at a loading rate of 10 mN/s; the cross profile of the indents after nanoindentation for as-cast (e) and ultrasonic-vibrated (f) $Pd_{40}Cu_{30}P_{20}Ni_{10}$ MGs in AFM images.

the reported U- [34], Zr- [18], and Fe-based [21,22] MGs.

To quantify the anelastic component of a creeping process, the relaxation time spectrum has been analyzed by means of [35]:

$$L(\tau)=\left[\sum_{i=1}^{n}\left(1+\frac{t}{\tau_i}\right)\frac{h_i}{\tau_i}e^{-t/\tau_i}\right]\frac{A_0}{P_0h_{in}}t|_{t=2\tau} \tag{5}$$

where L is the spectrum intensity, A_0/P_0 the inverse of the hardness H, and h_{in} the maximum indentation depth. Fig. 5 (a) and (b) display relaxation spectra of as-cast and ultrasonic-vibrated samples as a function of loading rates. Two distinct relaxation peaks can be identified clearly in relaxation spectra.

With increasing loading rates from 0.5 to 100 mN/s, both the intensity and characteristic relaxation time of the first and second peaks alter remarkably, implying the variation of the number of defects. Based on the core-shell model [28], the defects with more free volume can be defined as a flow unit. Corresponding to an anelastic deformation process of MGs, the flow unit can be well described by using Kelvin dash-pot [14,34], see Fig. 6. Two characterize relaxation time indicates that two kinds of flow units are provoked. As demonstrated in Fig. 6 (b), the first Kelvin unit with short average relaxation time represents the hard regime with small defects, while the second unit with longer average relaxation time represents the soft regime with large defects, corresponding to a loosened packing state. According to the derived data in Fig. 5, it is seen that both relaxation processes with short and long relaxation time of the as-cast sample are less pronounced as compared with the ultrasonic-vibrated sample, in line with its higher H and E as well as weaker creep deformation. More interestingly, for the sample after high-frequency mechanical vibration, the first peak that represents the relaxation process with shorter relaxation time become more intense at the loading rate higher than 10 mN/s, see Fig. 5 (b). The significant increase of the first relaxation peak of the softened sample after treated

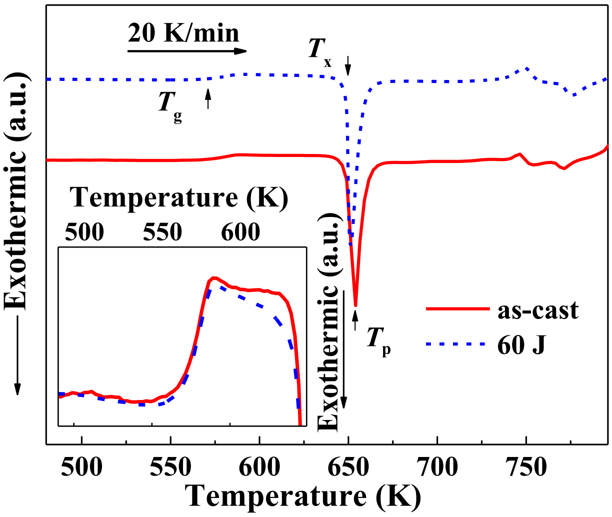

Fig. 8. DSC curves of the ultrasonic-vibrated $Pd_{40}Cu_{30}P_{20}Ni_{10}$ MG with the applied energy of 60 J at a heating rate of 20 K/min. The data for the as-cast sample were plotted for comparison. The inset shows the enthalpy recovery measurement.

by the high-frequency mechanical vibration indicates the activation of a large number of defects with small size. It suggests that the participation of the relaxation process with short relaxation time is more essential in the process of the creep flow.

To demonstrate the localized plastic deformation of Pd-based MGs after severely vibrated deformation, AFM images around the indents at the loading rate of 10 mN/s are displayed in Fig. 7(a)–(d). Several partial circle shear bands are found in the pile-up region around the indent of both as-cast and ultrasonic-vibrated samples, see Fig. 7(a) and (c). This phenomenon is ascribed to the obvious serration flow together with the propagation of shear bands during the initial loading period as demonstrated in *P-h* curves (Fig. 3 (a) and (b)). By using topographic profiles, see Fig. 7(e) and (f), we can precisely evaluate the pile-up around the indent, see Fig. 7 (b) and (d). The maximum height of the pile-up around indents of the vibrated sample is about 144 nm at the loading rate of 10 mN/s, which is 48% higher than 97 nm of the as-cast sample. It is shown that the pile-up around indents is more notable for the ultrasonic-vibrated sample, which indicates pronounced local plastic deformation after ultrasonic vibration. At the same loading rate, the maximum penetration depth derived from the topographic profile of the ultrasonic-vibrated sample is about 377 nm, which is slightly lower than 409 nm of the as-cast sample. This is consistent with the observation in $[(Co_{0.7}Fe_{0.3})_{0.68}B_{0.219}Si_{0.051}Nb_{0.05}]_{100-x}Cu_x$ (x = 0, 0.5) [21], where the sample with more significant plastic flow exhibits less penetration depth. It illustrates a more homogeneous deformation after vibration, which coincides with a slightly wider indentation area as found in Fig. 7 (f).

Fig. 8 shows DSC curves of as-cast and 60 J ultrasonic-vibrated MG samples. A glass transition feature and crystallization event(s) in DSC traces at a heating rate of 20 K/min can be seen clearly for both samples, which further proves the fact that the sample still maintains glassy state after 60 J mechanical vibration treatment. The glass transition temperature T_g, crystallization temperature T_x, and the supercooled region $\Delta T_x = (T_x - T_g)$ marked in Fig. 8 are listed in Table 3. It is seen that T_g, T_x, and ΔT_x almost keep a constant value after ultrasonic vibration. The magnified view of the thermal traces near T_g as shown in the inset of Fig. 8 gives the amount of the exothermic heat ΔH_{rel} [36]. The weak increase of relaxation enthalpy ΔH_{rel} after vibration is observed, which implies the excess free volume (Δv) derived by $\Delta v \propto \Delta H_{rel} = \int (dQ/dt) dT$ [37,38] hasn't changed too much after ultrasonic vibration as well.

By evaluating the dependence of thermodynamic parameters such as T_g, T_x and peak temperature (T_p) on the heating rate (θ), see Fig. 9, we can deduce the activation energies E_c (i.e., E_g, E_x, and E_p) for the glass transition or crystallization of MGs in non-isothermal heating mode according to the Kissinger plots [39]:

$$ln\left(\frac{T^2}{\theta}\right) = \frac{E_c}{RT} + ln\left(\frac{E_c}{k_0 R}\right) \tag{6}$$

where T is the temperature, R the gas constant, and k_0 the frequency factor. An approximate linear relation of the ln (T^2/θ) - 1000/T plot is displayed in Fig. 10. The activation energy for the glass transition E_g that determined by the slope of E_c/R in Eq. (3) is 530 ± 32 and 344 ± 34 kJ/mol for as-cast and 60 J MG samples, respectively. The derived E_g of the as-cast $Pd_{40}Cu_{30}P_{20}Ni_{10}$ MG in present work is close to that reported in Fe-based MGs like $Fe_{75}Mo_5P_{10}C_{7.5}B_{8.5}$ (435.6 kJ/mol) [40], which is much higher as compared with other MGs at their as-quenched state, such as $Cu_{46}Zr_{45}Al_7Y_2$ (361 kJ/mol) [41], $Ti_{41.5}Cu_{42.5}Zr_{2.5}Hf_5Ni_{7.5}Si_1$ (293 kJ/mol) [40], and $U_{64}Co_{28.5}Al_{7.5}$ MGs (338 kJ/mol) [42]. However, E_g of $Pd_{40}Cu_{30}P_{20}Ni_{10}$ MG decreases about 35% after ultrasonic vibration. Significant reduction of E_g implies the energy barrier for atomic diffusion during the glass transition decreases obviously owing to the softening effect of ultrasonic-assistant mechanical vibration. It indicates a higher potential energy state of the ultrasonic-vibrated sample with more activated defects, see the schematic in Fig. 6(b), which effectively improves atomic mobility in the vibrated samples. The activation energy for nucleation E_x also decreases from 270 ± 9 to 243 ± 2 kJ/mol after vibration, which suggests that the incubation time for nucleation is shortened. This is associated with the appearance of multiple nucleation sites as a result of the rearrangement of atomic configurations accompanied with the generation of large amount of small defects as demonstrated in relaxation time spectra, see in Figs. 5 and 6.

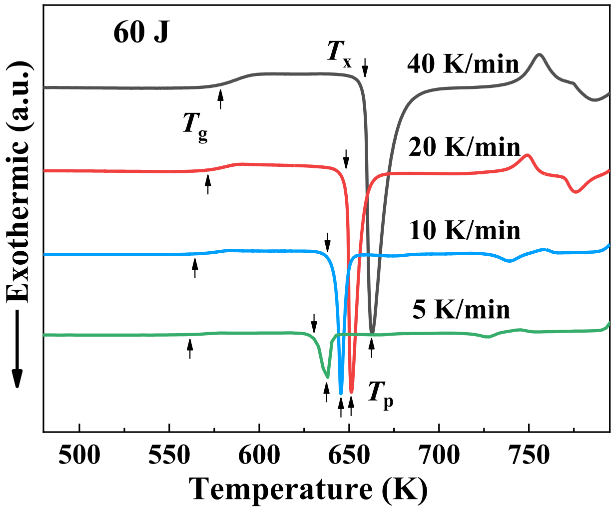

Fig. 9. DSC traces of the 60 J ultrasonic-vibrated MG at heating rates ranging from 5 to 40 K/min.

Table 3
Thermal properties of as-cast and 60 J ultrasonic-vibrated $Pd_{40}Cu_{30}P_{20}Ni_{10}$ MG samples, respectively.

	T_g (K)	T_x (K)	ΔT (K)	ΔH (kJ/mol)	E_g (kJ/mol)	E_x (kJ/mol)	E_p (kJ/mol)
As-cast	571	650	79	3.891	530 ± 32	270 ± 9	267 ± 19
60 J	571	649	78	3.869	344 ± 34	243 ± 2	274 ± 9

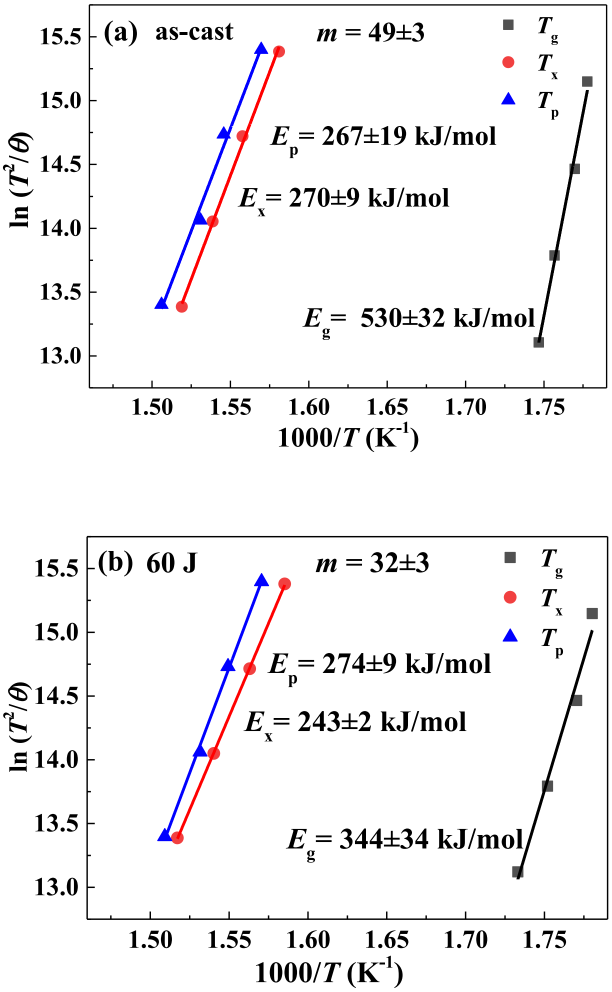

Fig. 10. Kissinger plots, the calculated activation energies relative to T_g, T_x, and T_p, and the fragility parameter m of as-cast (a) and 60 J ultrasonic-vibrated (b) $Pd_{40}Cu_{30}P_{20}Ni_{10}$ MG samples, respectively.

While the activation energy for the growth of the crystal nucleus E_p of the as-cast $Pd_{40}Ni_{10}Cu_{30}P_{20}$ MG is 267 ± 19 kJ/mol, which is slightly higher than the reported 228 kJ/mol in previous work of Zhao [40]. Such variety of E_p might be due to the narrow heating rate range (5–40 K/min) of our fitting procedure. It has been reported that the activation energy increases of ~36% when the scanning-rate range changes from 25 to 65 K/min to 5–20 K/min [43]. After ultrasonic vibration, E_p increases slightly from 267 ± 19 to 274 ± 9 kJ/mol. It proposes that the crystallization behavior of the Pd-based MG samples is impeded after ultrasonic vibration. The reduction of high-density amorphous phase as indicated by the activation of small defects under cycling loading leads to the fact that the formation of the polycrystalline structure becomes more difficult [44].

Based on E_g and T_g, the fragility parameter m can be derived [45]:

$$m = \frac{d\log\eta(T)}{d\left(T_g/T\right)}\Big|_{T=T_g} = \frac{E_g}{\ln 10 R T_g} \tag{7}$$

where $\eta(T)$ is the viscosity defined as $\eta(T) = \eta_0 exp(E/k_B T)$, η_0 the viscosity at the high-temperature limit, E the activation energy for viscous flow, and k_B Boltzmann's constant. The calculated m is 49 ± 3 and 32 ± 3 for as-cast and 60 J samples, respectively, see Fig. 10. Follow the definition of Angell, the value of m is small for strong liquids such as SiO_2 (m ~ 16) with directional atomic bonding and large for fragile liquids like o-terphenyl (m ~ 150) [46]. Similar to Ce-based (m ~ 32–34) [47] and U-based (m ~ 28) [42] MGs, the investigated as-cast Pd-based MG with m of 49 can be classified as a relatively fragile metallic glass-forming system. However, after ultrasonic vibration with the energy of 60 J, a much stronger behavior with m of a lower value of 32 is found in the $Pd_{40}Cu_{30}P_{20}Ni_{10}$ MG. It implies that the cycling deformation at ultrasonic-frequency obviously alters the viscous flow behavior of the Pd-based MG system with a relatively low T_g (~571 K, around 300 K higher than the ambient temperature). This phenomenon may be ascribed to the dramatic reduction of the energy barrier for atomic diffusion during the glass transition of ~35% as demonstrated in DSC traces. Therefore, the ultrasonic-assistant superplastic flow during nano- to micro-molding and imprinting [1,2,11] or cold joining [7] in Pd-based MGs might be interrelated to the mechanical glass transition as a result of stress-induced structural rearrangement. As proposed in the work of Ketkaew et. Al., the brittle-to-ductile transition revealed by fracture toughness is associated with the structure relaxation at the fictive temperature that approach T_g due to the non-equilibrium state of MGs [48]. Differ from their work, the mechanical softening observed in our studies results from the stress-induced structure evolution under cycling loading [6], rather than the temperature effect, which can promote the activation of flow defects during plastic deformation at ambient temperature, instead of the temperature that close to T_g.

On the other hand, it is found in DSC traces that the variety of excess free volume Δv in $Pd_{40}Cu_{30}P_{20}Ni_{10}$ MGs before and after ultrasonic vibration is not significant. It proposes that the free volume generated during vibration treatment almost annihilates at the same time. In other words, the activation of small defects as shown in Fig. 5 is accompanied with consumption of the existent large inherent defects. This process might lead to more homogenous structure along with stronger behavior as demonstrated by relatively low m shown in DSC analysis [49]. The activation of large amounts of small defects in the ultrasonic-vibrated sample is bounds up with the pronounced local plastic deformation around the indent and the associated softening behavior, see Fig. 7. It means that the stress-induced defect redistribution as shown in the relaxation time spectrum (i.e., structural heterogeneity), rather than structure rejuvenation along with increasing Δv as reported in severe plastic deformation MG systems [50,51], may account for the dramatic reduction of H and E in the ultrasonically vibrated $Pd_{40}Cu_{30}P_{20}Ni_{10}$ MG. The softening of $Pd_{0.775}Si_{0.165}Cu_{0.06}$ MG reported in the work of Golding et al. is relative to the possibility of non-uniform changes in the local atomic density in the slightly looser structure [52]. It well explains our nanoindentation and DSC results that the local atomic rearrangement induced by high-frequency mechanical vibration may promote a nonuniform redistribution of free volume in Pd-based MGs, which can be illustrated by the propagation of small defects as demonstrated by the distinguished relaxation processes with shorter characteristic time. The activated flow defects with short relaxation time play a dominant role in cutting down the resistance to shear, which eventually leads to the evident mechanical softening during ultrasonic-assistant plastic deformation. The improved magnitude of nonuniform atomic displacements due to the local intrinsic density fluctuation of glassy matrix can affect the vibration frequency of phonons [53]. It induces the reduced frequencies of transverse acoustic phonons. It seems like the flow defects with short relaxation time have a stronger intendency to involve in such soft transverse acoustic phonon process. Alternately, a notable reduction in E along with the decrease of viscosity during viscoplastic deformation might arise from the softening of long-wavelength transverse acoustic phonons in MGs under high-frequency cycling loading.

4. Conclusion

The micro-creep behaviors of the $Pd_{40}Cu_{30}P_{20}Ni_{10}$ MG after ultrasonic-vibration treatment with the applied energy of 60 J were investigated by using nanoindentation. The underlying mechanism for the defect activation at ambient temperature was well understood under the frame of the Maxwell-Voigt model. It is found that the provocation of flow defects under cycling loading benefits the structure relaxation at distinct characteristic time. Further data analysis based on the relaxation time spectrum demonstrates that the high defect concentration with short characteristic relaxation time is associated with the reduction of the activation energy for atomic diffusion during glass transition as well as the nucleation of crystals. It eventually leads to the inhomogeneous local plastic deformation, thereby large creep displacement along with a low viscosity during viscoplastic deformation, of the ultrasonic-vibrated sample. It might be the reason beneath that causes the significantly reduced *H* and *E* as well. Our work provides a clear picture of the ultrasonic-assistant structural rearrangement in non-equilibrium-state MGs based on their anelastic creep response, which may enlighten the physical origin of the superplastic flow in the glassy system during stress-assisted molding and cold joining process.

CRediT authorship contribution statement

Chenchen Yuan: Conceptualization, Investigation, Supervision, Writing - original draft, Writing – review & editing, Funding acquisition. **Rui Liu:** Investigation, Formal analysis. **Zhuwei Lv:** Investigation, Formal analysis. **Xin Li:** Resources. **Changmeng Pang:** Investigation. **Can Yang:** Resources. **Jiang Ma:** Supervision, Writing - review & editing. **Weihua Wang:** Writing - review & editing.

Declaration of competing interest

The authors declare that they have no known competing financial interests or personal relationships that could have appeared to influence the work reported in this paper.

Acknowledgements

This work was supported by the National Natural Science Foundation of China (Grant Nos. 52071078 and 51871157), the “Zhishan” Scholars Programs of Southeast University (Grant No. 2242021R41158), Postgraduate Research & Practice Innovation Program of Jiangsu Province (Grant No. SJCX20_0038), Jiangsu Key Laboratory for Advanced Metallic Materials (Grant No. BM2007204).

References

[1] G. Kumar, H.X. Tang, J. Schroers, Nanomoulding with amorphous metals, Nature 457 (7231) (2009) 868–872.

[2] G. Doubek, R.C. Sekol, J.Y. Li, W.H. Ryu, F.S. Gittleson, S. Nejati, E. Moy, C. Reid, M. Carmo, M. Linardi, P. Bordeenithikasem, E. Kinser, Y.H. Liu, X. Tong, C. O. Osuji, J. Schroers, S. Mukherjee, A.D. Taylor, Guided evolution of bulk metallic glass nanostructures: a platform for designing 3D electrocatalytic surfaces, Adv. Mater. 28 (10) (2016) 1940–1949.

[3] G.C. Han, Z. Peng, L.H. Xu, N. Li, Ultrasonic vibration facilitates the microformability of a Zr-based metallic glass, Materials 11 (12) (2018) 2568.

[4] F. Luo, F. Sun, K. Li, F. Gong, X. Liang, X. Wu, J. Ma, Ultrasonic assisted microshear punching of amorphous alloy, Mater. Res. Lett. 6 (10) (2018) 545–551.

[5] Y.M. Huang, Y.S. Wu, J.Y. Huang, The influence of ultrasonic vibration-assisted micro-deep drawing process, Int. J. Adv. Manuf. Technol. 71 (5–8) (2014) 1455–1461.

[6] Z.Y. Zhou, H.L. Peng, H.B. Yu, Structural origin for vibration-induced accelerated aging and rejuvenation in metallic glasses, J. Chem. Phys. 150 (20) (2019) 7.

[7] J. Ma, C. Yang, X. Liu, B. Shang, Q. He, F. Li, T. Wang, D. Wei, X. Liang, X. Wu, Y. Wang, F. Gong, P. Guan, W. Wang, Y. Yang, Fast surface dynamics enabled cold joining of metallic glasses, Sci. Adv. 5 (11) (2019), eaax7256.

[8] W.H. Wang, Correlations between elastic moduli and properties in bulk metallic glasses, J. Appl. Phys. 99 (9) (2006), 093506.

[9] W.H. Wang, The elastic properties, elastic models and elastic perspectives of metallic glasses, Prog. Mater. Sci. 57 (3) (2012) 487–656.

[10] J.J. Lewandowski, W.H. Wang, A.L. Greer, Intrinsic plasticity or brittleness of metallic glasses, Phil. Mag. Lett. 85 (2005) 77–87.

[11] B. Xu, X.Y. Wu, J. Ma, X. Liang, J.G. Lei, B. Wu, S.C. Ruan, Z.L. Wang, Micro-electrical discharge machining of 3D micro-molds from $Pd_{40}Cu_{30}P_{20}Ni_{10}$ metallic glass by using laminated 3D micro-electrodes, J. Micromech. Microeng. 26 (3) (2016), 035004.

[12] A. Concustell, J. Sort, A.L. Greer, M.D. Baro, Anelastic deformation of a $Pd_{40}Cu_{30}Ni_{10}P_{20}$ bulk metallic glass during nanoindentation, Appl. Phys. Lett. 88 (17) (2006) 171911.

[13] A.C. Fischer-Cripps, A simple phenomenological approach to nanoindentation creep, Mater. Sci. Eng. A 385 (1–2) (2004) 74–82.

[14] A. Castellero, B. Moser, D.I. Uhlenhaut, F.H.D. Torre, J.F. Löffler, Room-temperature creep and structural relaxation of Mg-Cu-Y metallic glasses, Acta Mater. 56 (2008) 3777–3785.

[15] Z.W. Lv, C.C. Yuan, H.B. Ke, B.L. Shen, Defects activation in CoFe-based metallic glasses during creep deformation, J. Mater. Sci. Technol. 69 (2021) 42–47.

[16] R. Maaß, P. Birckigt, C. Borchers, K. Samwer, C.A. Volkert, Long range stress fields and cavitation along a shear band in a metallic glass: the local origin of fracture, Acta Mater. (2015) 94–102.

[17] W.C. Oliver, G.M. Pharr, An improved technique for determining hardness and elastic modulus using load and displacement sensing indentation experiments, J. Mater. Res. 7 (6) (1992) 1564–1583.

[18] C.C. Yuan, Z.W. Lv, C.M. Pang, X. Li, R. Liu, C. Yang, J. Ma, H.B. Ke, W.H. Wang, B. L. Shen, Ultrasonic-assisted plastic flow in a Zr-based metallic glass, Sci. China Mater. 64 (2) (2021) 448–459.

[19] B.-G. Yoo, J.-H. Oh, Y.-J. Kim, K.-W. Park, J.-C. Lee, J.-i. Jang, Nanoindentation analysis of time-dependent deformation in as-cast and annealed Cu-Zr bulk metallic glass, Intermetallics 18 (10) (2010) 1898–1901.

[20] Y.J. Huang, J. Shen, Y.L. Chiu, J.J.J. Chen, J.F. Sun, Indentation creep of an Fe-based bulk metallic glass, Intermetallics 17 (4) (2009) 190–194.

[21] C.C. Yuan, Z.W. Lv, C.M. Pang, W.W. Zhu, X.-L. Wang, B.L. Shen, Pronounced nanoindentation creep deformation in Cu-doped CoFe-based metallic glasses, J. Alloys Compd. 806 (2019) 246–253.

[22] C.C. Yuan, R. Liu, C.M. Pang, X.F. Zuo, B.F. Li, S.C. Song, J.Y. Hu, W.W. Zhu, B. L. Shen, Anelastic and viscoplastic deformation in a Fe-based metallic glass, J. Alloy. Compd. 853 (2021) 157233.

[23] C.A. Schuh, T.G. Nieh, A nanoindentation study of serrated flow in bulk metallic glasses, Acta Mater. 51 (1) (2003) 87–99.

[24] C.A. Schuh, A.C. Lund, T.G. Nieh, New regime of homogeneous flow in the deformation map of metallic glasses: elevated temperature nanoindentation experiments and mechanistic modeling, Acta Mater. 52 (20) (2004) 5879–5891.

[25] R. Maaß, D. Klaumünzer, J.F. Löffler, Propagation dynamics of individual shear bands during inhomogeneous flow in a Zr-based bulk metallic glass, Acta Mater. 59 (2011) 3205–3213.

[26] R. Maaß, D. Klaumünzer, G. Villard, P.M. Derlet, J.F. Löffler, Shear-band arrest and stress overshoots during inhomogeneous flow in a metallic glass, Appl. Phys. Lett. 100 (2012), 071904.

[27] Y.H. Liu, G. Wang, R.J. Wang, D.Q. Zhao, M.X. Pan, W.H. Wang, Super plastic bulk metallic glasses at room temperature, Science 315 (5817) (2007) 1385–1388.

[28] J.C. Ye, J. Lu, C.T. Liu, Q. Wang, Y. Yang, Atomistic free-volume zones and inelastic deformation of metallic glasses, Nat. Mater. 9 (2010) 619–623.

[29] A.I. Taub, F. Spaepen, Ideal elastic, anelastic and viscoelastic deformation of a metallic glass, J. Mater. Sci. 16 (1981) 3087–3092.

[30] Y. Yang, J.F. Zeng, A. Volland, J.J. Blandin, S. Gravier, C.T. Liu, Fractal growth of the dense-packing phase in annealed metallic glass imaged by high-resolution atomic force microscopy, Acta Mater. 60 (2012) 5260–5272.

[31] C.C. Yuan, Z.W. Lv, C.M. Pang, X.L. Wu, S. Lan, C.Y. Lu, L.G. Wang, H.B. Yu, J. H. Luan, W.W. Zhu, G.L. Zhang, Q. Liu, X.-L. Wang, B.L. Shen, Atomic-scale heterogeneity in large-plasticity Cu-doped metallic glasses, J. Alloys Compd. 798 (2019) 517–522.

[32] P. Tsai, K. Kranjc, K.M. Flores, Hierarchical heterogeneity and an elastic microstructure observed in a metallic glass alloy, Acta Mater. 139 (2017) 11–20.

[33] B. Sarac, Y.P. Ivanov, A. Chuvilin, T. Schoberl, M. Stoica, Z.L. Zhang, J. Eckert, Origin of large plasticity and multiscale effects in iron-based metallic glasses, Nat. Commun. 9 (2018) 1333.

[34] H.B. Ke, R. Zhang, B.A. Sun, P.G. Zhang, T.W. Liu, P.H. Chen, M. Wu, H.G. Huang, Dissimilar nanoscaled structural heterogeneity in U-based metallic glasses revealed by nanoindentation, J. Alloy. Compd. 788 (2019) 391–396.

[35] D. John, Ferry, Viscoelastic Properties of Polymers, third ed., Wiley, 1980.

[36] A. Vandenbeukel, J. Sietsma, The glass-transition as a free-volume related kinetic phenomenon, Acta Metall. Mater. 38 (3) (1990) 383–389.

[37] A. Slipenyuk, J. Eckert, Correlation between enthalpy change and free volume reduction during structural relaxation of $Zr_{55}Cu_{30}Al_{10}Ni_5$ metallic glass, Scripta Mater. 50 (1) (2004) 39–44.

[38] C.C. Yuan, J. Ma, X.K. Xi, Understanding the correlation of plastic zone size with characteristic dimple pattern length scale on the fracture surface of a bulk metallic glass, Mater. Sci. Eng. A-Struct. Mater. Prop. Microstruct. Process. 532 (2012) 430–434.

[39] H.E. Kissinger, Reaction kinetics in differential thermal analysis, Anal. Chem. 29 (1957) 1702–1706.

[40] L. Zhao, H. Jia, S. Xie, X. Zeng, T. Zhang, C. Ma, A new method for evaluating structural stability of bulk metallic glasses, J. Alloys Compd. 504 (2010) S219–S221.

[41] J.C. Qiao, J.M. Pelletier, Crystallization kinetics in $Cu_{46}Zr_{45}Al_7Y_2$ bulk metallic glass by differential scanning calorimetry (DSC), J. Non-Cryst. Solids 357 (2011) 2590–2594.

[42] H.B. Ke, H.Y. Xu, H.G. Huang, T.W. Liu, P. Zhang, M. Wu, P.G. Zhang, Y.M. Wang, Non-isothermal crystallization behavior of U-based amorphous alloy, J. Alloys Compd. 691 (2017) 436–441.

[43] Z.Z. Yuan, X.D. Chen, B.X. Wang, Y.J. Wang, Kinetics study on non-isothermal crystallization of the metallic $Co_{43}Fe_{20}Ta_{5.5}B_{31.5}$ glass, J. Alloys Compd. 407 (2006) 163–169.

[44] V.L. Deringer, N. Bernstein, G. Csanyi, C. Ben Mahmoud, M. Ceriotti, M. Wilson, D. A. Drabold, S.R. Elliott, Origins of structural and electronic transitions in disordered silicon, Nature 589 (7840) (2021) 59–64.

[45] R. Bohmer, K.L. Ngai, C.A. Angell, D.J. Plazek, Nonexponential relaxations in strong and fragile glass formers, J. Chem. Phys. 99 (1993) 4201–4209.

[46] J.C. Dyre, Colloquium: the glass transition and elastic models of glass-forming liquids, Rev. Mod. Phys. 78 (2006) 953–972.

[47] T. Wang, Y.Q. Yang, J.B. Li, G.H. Rao, Thermodynamics and structural relaxation in Ce-based bulk metallic glass-forming liquids, J. Alloys Compd. 509 (2011) 4569–4573.

[48] J. Ketkaew, W. Chen, H. Wang, A. Datye, M. Fan, G. Pereira, U.D. Schwarz, Z. Liu, R. Yamada, W. Dmowski, M.D. Shattuck, C.S. O'Hern, T. Egami, E. Bouchbinder, J. Schroers, Mechanical glass transition revealed by the fracture toughness of metallic glasses, Nat. Commun. 9 (2018) 3271.

[49] M.D. Ediger, Spatially heterogeneous dynamics in supercooled liquids, Annu. Rev. Phys. Chem. 51 (2000) 99.

[50] J. Pan, Y.X. Wang, Q. Guo, D. Zhang, A.L. Greer, Y. Li, Extreme rejuvenation and softening in a bulk metallic glass, Nat. Commun. 9 (2018) 560.

[51] W. Dmowski, Y. Yokoyama, A. Chuang, Y. Ren, M. Umemoto, K. Tsuchiya, A. Inoue, T. Egami, Structural rejuvenation in a bulk metallic glass induced by severe plastic deformation, Acta Mater. 58 (2) (2010) 429–438.

[52] B. Golding, F.S.L. Hsu, B.G. Bagley, Soft transverse phonons in a metallic glass, Phys. Rev. Lett. 29 (1) (1972) 68–70.

[53] W.H. Wang, H.Y. Bai, J.L. Luo, R.J. Wang, D. Jin, Supersoftening of transverse phonons in $Zr_{41}Ti_{14}Cu_{12.5}Ni_{10}Be_{22.5}$ bulk metallic glass, Phys. Rev. B 62 (1) (2000) 25–28.